Taylor & Francis
Taylor & Francis Group

FOCUS ISSUE ARTICLE

🔓 OPEN ACCESS | Check for updates

Framework confinement of multi-metals within silica hollow spheres by one-pot synthesis process

Wenli Zhao[a]*, Yangfeng Liu[a]*, Ao Li[b]*, Fancang Meng[a], Yang Du[b] and Qingmin Ji[a]

[a]School of Materials Science and Engineering, Herbert Gleiter Institute for Nanoscience, Nanjing University of Science and Technology, Nanjing, P. R. China;
[b]School of Chemical Engineering, Nanjing University of Science and Technology, Nanjing, P. R. China

ABSTRACT

The control incorporation of metals in silica hollow spheres (SHSs) may bring new functions to silica mesoporous structures for applications including catalysis, sensing, molecular delivery, adsorption filtration, and storage. However, the strategies for incorporating metals, whether through pre-loading in the hollow interior or post-encapsulation in the mesoporous shell, still face challenges in achieving quantitative doping of various metals and preventing metal aggregation or channel blockage during usage. In this study, we explored the doping of different metals into silica hollow spheres based on the dissolution-regrowth process of silica. The process may promote the formation of more structural defects and functional silanol groups, which could facilitate the fixation of metals in the silica networks. With this simple and efficient approach, we successfully achieved the integration of ten diverse metal species into silica hollow sphere (SHS). Various single-metal, dual-metal, triple-metal, and quadruple-metal doped SHSs have been prepared, with the doped metals being stable and homogeneously dispersed in the structure. Based on the structural characterizations, we analyzed the influence of metal types on the morphology features of SHSs. The synergistic effects of multi-metals on the catalysis applications were also studied and compared.
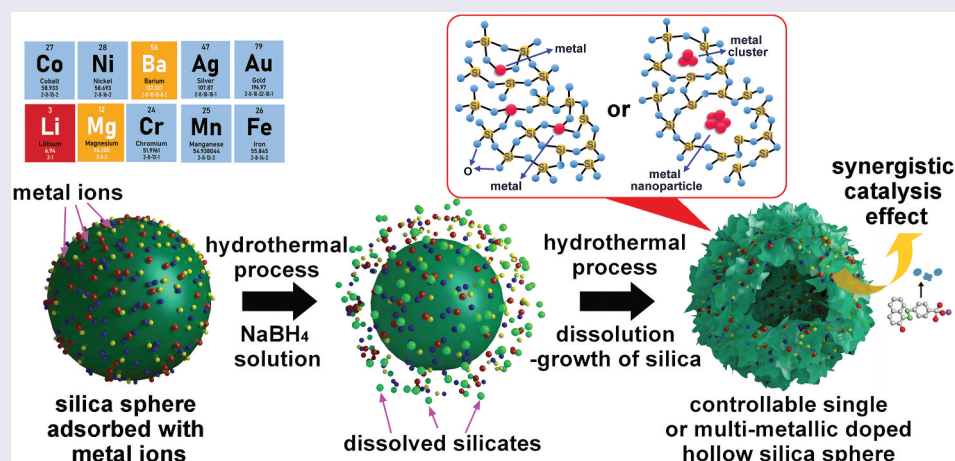
IMPACT STATEMENT

Significance of this work: The control incorporation of metals in silica hollow spheres (SHSs) may bring new functions to silica mesoporous structures for applications including catalysis, sensing, molecular delivery, adsorption filtration, and storage. The incorporation of metals within SHSs is always either at the interior core or in the porous shells. The former method mainly utilizes metal nanoparticles as the core and regulates the synthesis of outer porous silica shells. The latter is primarily driven by the capillary force or intermolecular interactions with surface ligands to facilitate the post-loading of metal species in porous silica structures. The main problems associated with metal-doped SHSs include 1) controlled loading of different metals with a homogeneous distribution; 2) fixation of metal species in the structures to prevent aggregation during usage, particularly at high temperatures; 3) pore channel blockage after metal loading, which may hinder the loading of other external molecules. In this work, we

CONTACT Qingmin Ji ✉ jiqingmin@njust.edu.cn 🖃 School of Materials Science and Engineering, Herbert Gleiter Institute for Nanoscience, Nanjing University of Science and Technology, 200 Xiaolingwei, Nanjing 210094, P. R. China; Yang Du ✉ duy@njust.edu.cn 🖃 School of Chemical Engineering, Nanjing University of Science and Technology, Nanjing 210094, P. R. China.

*The authors contributed equally to this work.

🔓 Supplemental data for this article can be accessed online at https://doi.org/10.1080/14686996.2024.2309912.

developed the dissolution-regrowth of silica strategy for integrating various metals in porous SHSs (M@SHSs) by a one-pot hydrothermal process without using any anchoring molecules. Unlike other sol-gel formations, the growth rate of silica in this process is greatly reduced. It thus may bring more possibilities to introduce external metals within the silica frameworks instead of in the porous channels. By regulating the addition of metal salts in the silica nanoparticles dispersions, we have successfully synthesized stable and highly homogeneous single-metal, dual-metal, triple-metal, and quadruplemetal doped SHSs. Based on the structural characterizations, we analyzed the influence of metal types on the morphology features of SHSs. The synergistic effects of multi-metals on the catalysis applications were also studied and compared. Our results offer a facile and effective strategy for preparing multi-metals as nano-catalysts. Through proper design of the doped metals in SHSs, the structures should find more applications in catalysis, drug delivery, and adsorption with unique and enhanced properties.

1. Introduction

In the past few decades, hollow spherical structures have garnered considerable attention across various application fields, making them one of the most fascinating structural classes. These versatile structures have found applications in catalysis, energy storage, biomedical research, environmental remediation, sensors, and nanodevices [1–5]. Among various materials, silica possesses several advantages, including its abundance in the earth, high thermal stability, controllable morphological features, easy chemical modifications, and low cost.

The common strategies for the synthesis of silica hollow spheres (SHSs) always rely on the use of soft or solid templates, which involve surfactants, polymers, biomaterials, inorganic particles [6–8], *etc*. After removing the templates through dissolution or calcination, hollow interiors with dimensions ranging from micrometers to several tens of nanometers could be obtained. Based on the dissolution process of silica in basic conditions, self-template strategies can also lead to the formation of SHSs [9,10]. This type of fabrication may effectively avoid using expensive template molecules or solvents, simplify synthesis procedures, and largely maintain surface silanol groups for further functionalizations.

On the other hand, as silica is generally inert without optical and electrical properties, the incorporation of metals is one of the most effective pathways to bring functions to silica structures [11,12]. The doped metals may well confine in the nano-spaces of silica supports and thus exhibit improved or unique application properties. For example, Trogler et al. revealed that the Fe-doped SHSs have enhanced biodegradability for biomedical applications [13]; Jiang et al. successfully developed alkaline earth metal-doped hollow silica/titania spheres with enhanced electrorheological activity, which can be attributed to the improved dispersion stability and dielectric properties due to the hollow morphology and the metal-dopings [14]; Zhang and Dai et al. constructed an exceptional size-selective catalysis system based on Pd clusters encapsulated SHSs [15].

The incorporation of metals within SHSs is always either at the interior core or in the porous shells. The former method mainly utilizes metal nanoparticles as the core and regulates the synthesis of outer porous silica shells. The latter is primarily driven by the capillary force or intermolecular interactions with surface ligands to facilitate the post-loading of metal species in porous silica structures. The main problems associated with metal-doped SHSs include 1) controlled loading of different metals with a homogeneous distribution; 2) fixation of metal species in the structures to prevent aggregation during usage, particularly at high temperatures; 3) pore channel blockage after metal loading, which may hinder the loading of other external molecules. The development of controllable, stable fixed atomic or cluster levels active metals in SHSs is still expected for further exploration of application potentials.

In our previous studies, we found that the porous silica nanostructures from the dissolution-regrowth process may possess more structural defects and functional silanol groups in the structures, which favor the fixation of metal components in the structures [16–18]. Unlike other sol-gel formations, the growth rate of silica is greatly reduced in this hydrothermal process. It thus may bring more possibilities to introduce external metals within the silica frameworks instead of in the porous channels.

Herein, we developed this dissolution-regrowth strategy for integrating various metals in porous SHSs (M@SHSs) by a one-pot hydrothermal process without using any anchoring molecules (Figure 1). By regulating the addition of metal salts and silica nanoparticles into a sodium borohydride ($NaBH_4$) solution, we have successfully synthesized stable and highly homogeneous single-metal, dual-metal, triple-metal, and quadruple-metal doped SHSs. Based on the structural characterizations, we analyzed the influence of metal types on the morphology features of SHSs. The synergistic effects of multi-metals on the catalysis applications were also studied and compared. The work presents a facile and generic pathway to control the doping of multiple atomic or cluster metals in porous silica spheres. With hollow architecture and
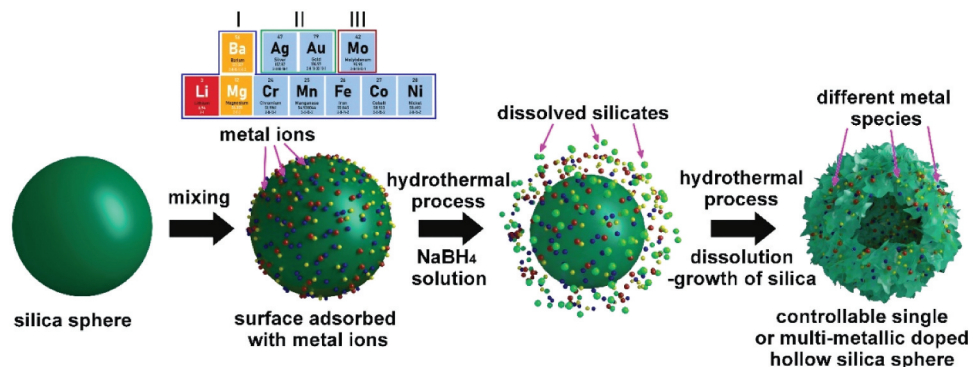
Figure 1. The scheme for the controllable fabrication of different single- or multi-metallic doped silica hollow spheres by one-pot synthesis process. I type of metals could be intercalated into silica frameworks; II type of metals doped as nanocluster or nanoparticles in the porous space of the silica; III type of metal may influence aggregation and regrowth structures of silica.

large surface area, the active metals in the structure could access external molecules easily. The application potentials of porous silica may also further be explored through the incorporation of different metals.

2. Materials and methods

2.1. Materials

Tetraethyl orthosilicate (TEOS, 99.0%, Aldrich), ammonia solution ($NH_3 \cdot H_2O$, 25–28 wt%, Aldrich), ferric chloride ($FeCl_3$, 99.0%, Macklin), cobaltous chloride hexahydrate ($CoCl_2 \cdot 6 H_2O$, 99.0%, Macklin), manganese chloride tetrahydrate ($MnCl_2 \cdot 4 H_2O$, 99.0%, Macklin), magnesium chloride ($MgCl_2 \cdot 6 H_2O$, 99.0%, Macklin), barium chloride ($BaCl_2$, 99.0%, Macklin), nickel chloride hexahydrate ($NiCl_2 \cdot 6 H_2O$, 99.0%, Macklin), lithium chloride hydrate ($LiCl \cdot H_2O$, 99.0%, Macklin), chromium(III) nitrate nonahydrate ($Cr(NO_3)_3 \cdot 9 H_2O$, 99.99%, Macklin), molybdenum chloride ($MoCl_5$, 99.5%, Macklin), silver chloride ($AgCl$, 99.99%, Macklin), chloroauric (III) acid tetrahydrate ($HAuCl_4 \cdot 4 H_2O$, 99.0%, Sinopharm) and sodium borohydride ($NaBH_4$, 99.5%, Sigma-Aldrich), were used as received. Deionized water (DI) used in the experiments was purified through a Pure-lab Prima system to a resistivity of $18.2 \, M\Omega \cdot cm^{-1}$.

2.2. Fabrication of metal doped silica hollow spheres

The SiO_2 nanospheres approximately 500 nm in diameter, were synthesized by the Stöber method. The metal-doped porous silica was prepared through a one-pot hydrothermal process. Typically, SiO_2 spheres (150 mg) and metal salts (0.1 mmol) were added to 5 mL of deionized water. The mixture solution was ultrasonicated for 10 minutes. The metal ions should adsorb onto the surface of SiO_2 through electrostatic interaction. $NaBH_4$ (500 mg) was added to the mixture under stirring.

The mixture solution was transferred into a Teflon-lined stainless autoclave with a capacity of 20 mL and kept at 140°C for 20 h. The products were collected by centrifugation and washing with deionized water until the washings were of neutral pH. The samples were finally dried with a freeze-dryer. $FeCl_3$, $CoCl_2 \cdot 6 H_2O$, $MgCl_2 \cdot 6 H_2O$, $MnCl_2 \cdot 4 H_2O$, $BaCl_2$, $NiCl_2 \cdot 6 H_2O$, $LiCl \cdot H_2O$, $Cr(NO_3)_3 \cdot 9 H_2O$, $AgCl$, $HAuCl_4 \cdot 4 H_2O$, and $MoCl_5$ were used as metal precursor. The capable formed metal-doped silica hollow spheres were named as Fe@SHS, Co@SHS, Mg@SHS, Mn@SHS, Ba@SHS, Ni@SHS, Li@SHS, Cr@SHS, Ag@SHS, and Au@SHS, respectively.

2.3. Characterization

The structural analysis of the synthesized samples was performed using powder X-ray diffraction (Brucker AXS D8 diffractometer, Germany) with copper as the target. The diffraction measurement was conducted over a 2θ range of 10–80°. Morphological studies of the samples were conducted using a scanning electron microscope (SEM, JSM-IT500HR, Japan) at 15 kV and transmission electron microscopy (TEM, JEOL, JEM-2100F, Japan) at 200 kV. Elemental analysis was carried out using an energy-dispersive X-ray analysis facility coupled with the TEM instrument. The specific surface area of the samples was obtained by the Brunauer-Emmett-Teller (BET) method using N_2 adsorption at 77 K on a Quanta chrome instrument (United States). The mesopore distributions were analyzed by using the Barrett-Joyner-Halenda (BJH) method, based on the adsorption branch of the N_2 isotherm. UV-vis spectra were measured using a Shimadzu UV-3600 spectrometer (Japan). Fourier transform infrared (FT-IR) spectra were obtained using a Nicolet iS10 FTIR spectrometer (Thermo Fisher, United States). X-ray photoelectron spectroscopy (XPS) measurements were performed using a Thermo ESCALAB 250XI instrument (United States).

2.4. Catalysis performance of metal-doped SHSs

The catalytic activity of metal-doped silica hollow spheres (M@SHSs) was evaluated by degradation of acid orange 7 (AO7) with the presence of H_2O_2. Typically, the aqueous dispersion of M@SHSs with a concentration of 80 µg/ml was prepared and adjusted to pH = 5.5 by HCl solution. AO7 (0.3 mM) and H_2O_2 (1 mM) were then added into the dispersion and stirred for 2 hours. The absorbance values at λ_{max} = 484 nm were recorded for up to 5 minutes in time course mode on a UV-vis spectrophotometer (Shimadzu UV-3600, Japan). The concentration of AO7 solution was determined by analyzing the peak intensity at 484 nm.

The percentage conversion was calculated based on the UV-vis results using the following formula:

$$Conversion\% = \frac{A_0 - A_t}{A_0} \times 100$$

where A_0 is the absorbance at the time ($t = 0$) and A_t is the value of absorbance at the time (t) following the commencement of the reaction.

The reaction kinetics are considered to be pseudo-first order with respect to the concentration of AO7. The rate constant (k) for the pseudo-first-order reaction can be defined using the equation. The ratio of absorbance at time t (A_t) to that at the time $t = 0$ (A_0) is proportional to the ratio of concentrations at any time t (C_t) to that at the time $t = 0$ (C_0).

$$\ln \frac{C_t}{C_0} = \ln \frac{A_t}{A_0} = -k \times t$$

3. Results and discussion

3.1. Single-metal doped silica hollow spheres

The doping of metals in silica hollow spheres (SHSs) was based on the hydrothermal dissolution-regrowth process in $NaBH_4$ solution at 140°C. Silica solid particles could undergo a structural transformation into hollow spheres. $NaBH_4$ provides a basic condition leading to silica dissolution, while the produced BO_2^- anions can promote the regrowth of the saturated dissolved silicate precursors around the surface of the SiO_2 particles [19]. As the silica precursors are supplied gradually with the dissolution, the regrowth rate of the silica network is thus suppressed in contrast to the normal sol-gel reaction. It thus increases the chance for the incorporation of foreign metal in the silica framework.

Since the SiO_2 surface possesses a negative charge, metal ions may incline to adsorb on the silica surface by electrostatic force. We tried to directly mix various metal ions (Fe^{3+}, Co^{2+}, Mg^{2+}, Mn^{2+}, Ba^{2+}, Ni^{2+}, Li^+, Cr^{2+}, Au^{3+}, Ag^+, Mo^{5+}) with silica particles and carried out one-pot hydrothermal process for metal-doped

SHSs. The SEM and TEM observations indicated that although the morphology features were not the same, SHSs with the metal incorporation were formed for most cases (Figure 2).

From the TEM images (Figure 3), Mg-, Co-, Fe-, Mn-doped SHSs (Mg@SHS, Co@SHS, Fe@SHS, Mn@SHS) possessed quite similar hollow spheres to SHSs without the addition of metal ions, which shells were composed by silica nanoflakes. However, by careful comparison, the nanofeatures of the flake shells were different. The Mg@SHS showed thicker shell thickness and looser shell density than the SHS without metals. While the flakes of Co@SHS, Fe@SHS, and Mn@SHS became much smaller and more curly. There were no obvious heterogeneous nano-aggregates observed in the hollow spheres. However, the elemental mappings of these metal-doped SHSs confirmed the homogeneous distributions of Si, O, and Mg/Co/Fe/Mn in the structure (Figure 3).

The XRD patterns of these metal-doped SHSs revealed a broad peak centered around 23° from amorphous silica (Figure S1). The diffraction peaks of crystalline metals could hardly be detected, suggesting the doped metal species dispersed at the atomic or molecular cluster level within the hollow spheres.

For the cases of mixing with Au^{3+} and Ag^+, although hollow spheres were formed, we can observe tiny nanoparticles homogeneously dispersed in the flake shells (Figure S2(a–f)). The XRD patterns of Au@SHS and Ag@SHS indicated the crystalline nature of Au and Ag nanoparticles (Figure S2(g,h)). The size of the metal nanoparticles could vary from 2 nm to 10 nm according to the additional amount of metal precursors. Due to the confinement effect by the porous flakes, the encapsulated Au and Ag nanoparticles were well immobilized within the shells. Even when subjected to high-temperature treatment, no aggregation or fusion of the nanoparticles was detected [10].

The SHSs derived from the addition of Ba^{2+} exhibited a distinct hollow morphology compared to other metal-doped SHSs. As shown in Figure S3, Ba@SHS displayed a hollow sphere with two thin layered shells instead of a single flake-shelled sphere. The EDS analysis revealed a significantly lower presence of Ba elements in the spheres. In the case of mixing with Mo^{5+}, it was found that the transformation into hollow spheres was unsuccessful. Instead, only nanoparticle aggregates were observable (Figure 2(l)).

3.2. The supposed formation mechanisms of metal@SHSs

The above observations have indicated that the metal doping process of silica through dissolution-regrowth is a convenient strategy for incorporating a variety of nano-metals in SHSs. However, it also revealed that
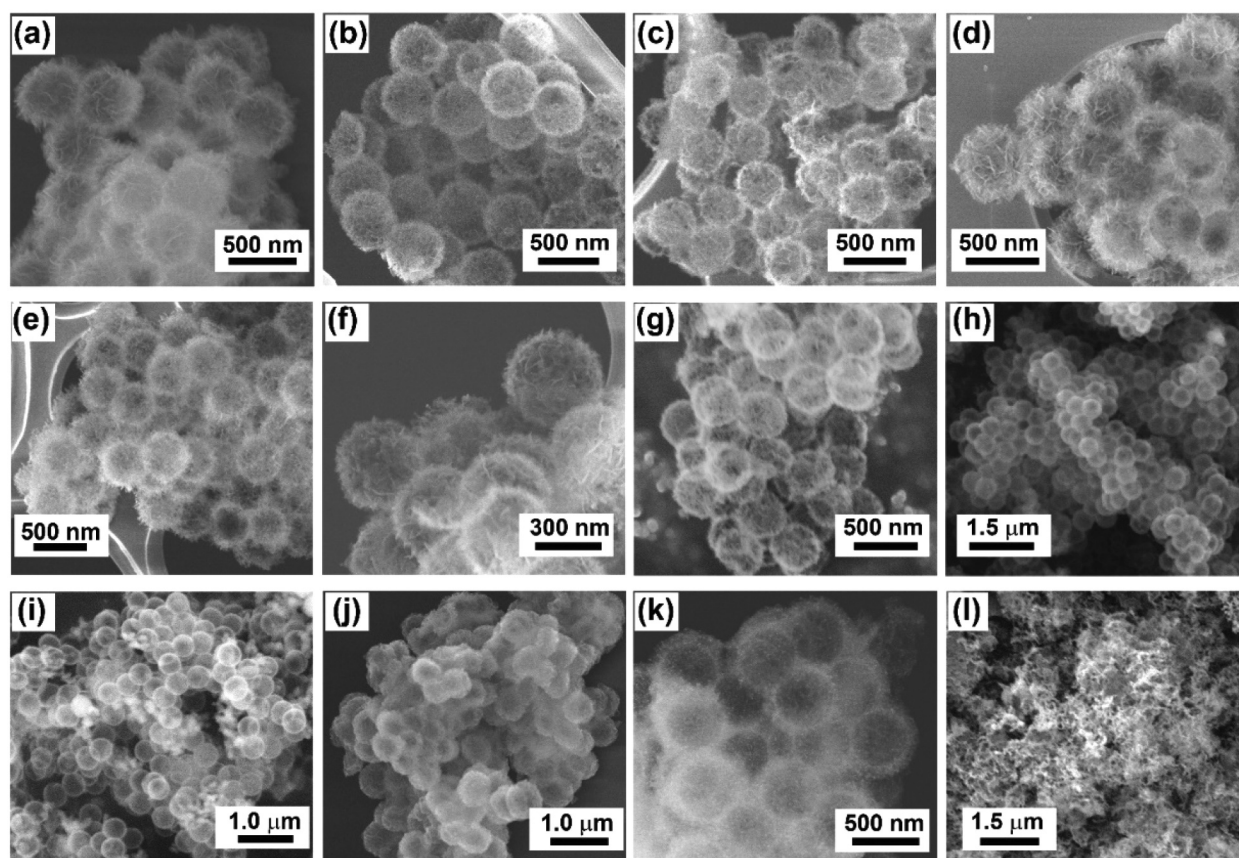
Figure 2. The SEM images for different metal-doped silica structures by the one-pot synthesis process. (a) silica hollow sphere without metals (SHS), (b) Fe-doped SHS (Fe@SHS), (c) Co-doped SHS (Co@SHS), (d) Mg-doped SHS (Mg@SHS), (e) Mn-doped SHS (Mn@SHS), (f) Ba-doped SHS (Ba@SHS), (g) Ni-doped SHS (Ni@SHS), (h) Li-doped SHS (Li@SHS), (i) Cr-doped SHS (Cr@SHS), (j) Ag-doped SHS (Ag@SHS), (k) Au-doped SHS (Au@SHS), (l) Mo-doped SHS (Mo@SHS).

the types of metal ions can influence the nanofeatures and the distribution states of metal in M@SHSs.

According to the appearance of the reaction solution and structural analyses, we suggested three in-situ formation pathways of the metal-doped silica structures by this one-pot hydrothermal process. The first type of M^I@SHSs showed flake-shelled SHSs with atomic or cluster metal species distributed in the shells (framework doping), which included Mg/Co/Fe/Mn/Ni/Cr/Li@SHSs. This kind of metal ions were inclined to form metal hydroxyl species in the reaction solution [20]. During the silica transformation process, metal hydroxyl species could interact with dissolved siloxy species and intercalate into silica networks (Figure 4). For metal with relatively larger radius, such as Ba^{2+}, although they may also form hydroxyl species during the reaction, they are difficult to penetrate within the siloxane network. They might just adsorb on the surface of silica layers by hydrogen bonding or electrostatic force. As $Ba(OH)_2$ can dissolve in water, the adsorbed Ba layer in the silica shells might wash away during collection and washing procedures. It thus led to the formation of two-shelled hollow spheres and less content of Ba element in the structure.

In the second pathway of the doped metals in M^{II}@SHSs, metal ions do not form metal hydroxyl

species, but directly reduce into zero valence metals. $NaBH_4$ is a highly effective reducing agent that is widely utilized in the synthesis of metal nanoparticles. Hence, when Au^{3+} and Ag^+ metal ions were present in the dispersion of silica particles, they can be reduced to Au^0 and Ag^0 directly during the reaction process. We can observe the color of silica particle dispersion with Au^{3+} or Ag^+ changed from light yellow to deep purple or dark brown after mixing with $NaBH_4$. The reduced Au and Ag in the dispersion could not return back to ionic states by forming hydroxyl species in the following hydrothermal process. The doped Au and Ag in the SHSs thus were in the form of Au and Ag nanoparticles. The fixation of the metal nanoparticles largely relies on the defects or nanopores in the silica network (porous trapping) (Figure 4). As the silica flakes grown from the hydrothermal process were thin (5–10 nm in thickness) [19], it caused the formation of more pores both in the flakes and from the aggregates of flakes. The special flaked shells provided a good confinement environment and effectively prevented the migration and fusion of the loaded nanoparticles during high-temperature treatment.

In the third pathway of metal doping through this one-pot process, the introduction of metal ions may significantly affect the growth environment of the silica
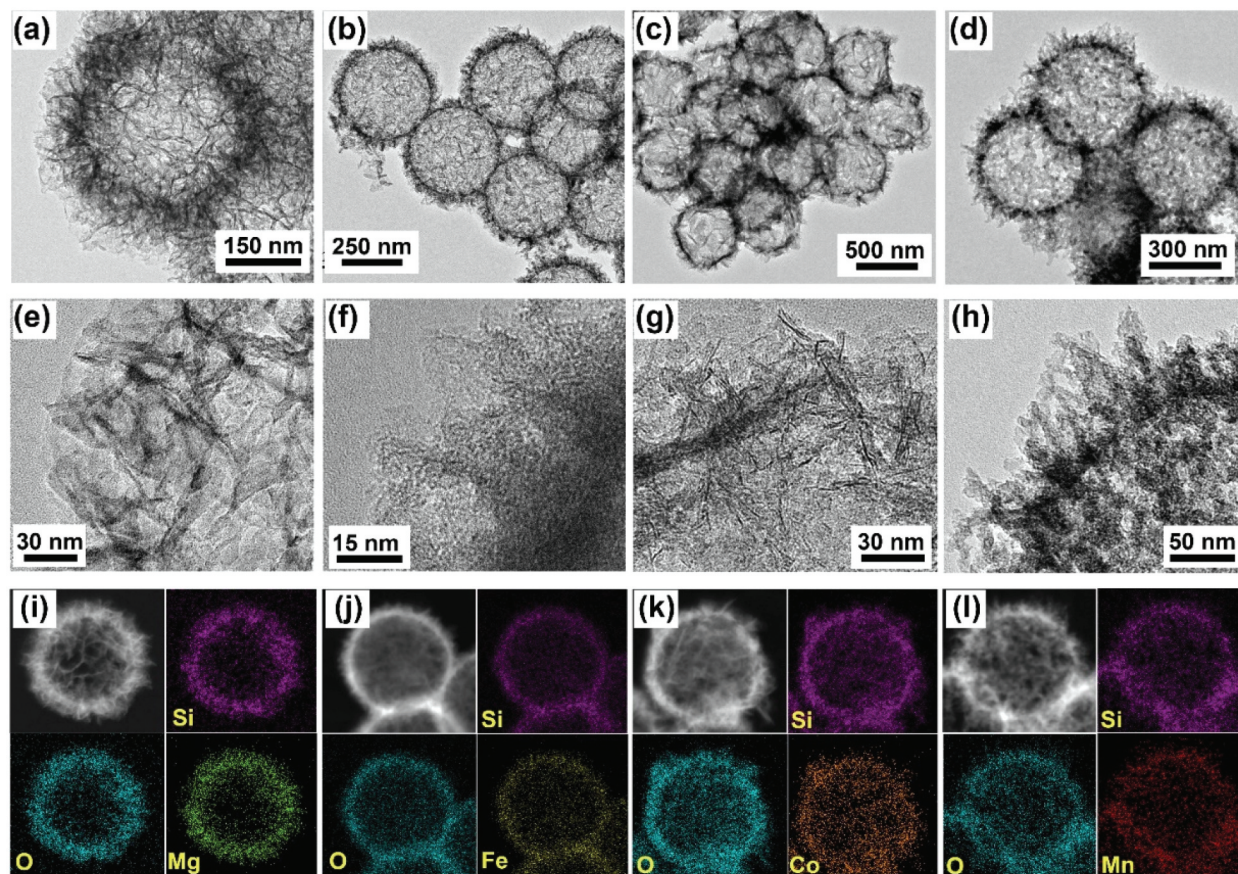
Figure 3. The TEM images of (a), (e) Mg@SHS; (b), (f) Mg@SHS; (c), (g) Co@SHS; (d), (h) Mn@SHS. The corresponding elemental mappings of (i) Mg@SHS; (j) Mg@SHS; (k) Co@SHS; (l) Mn@SHS.
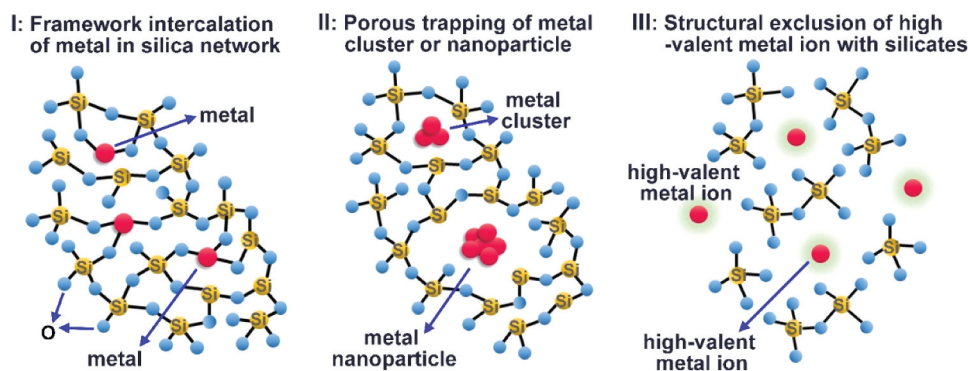

Figure 4. The supposed doping mechanisms of different types of metals in the silica structures.

network, impeding the formation of SHSs (structural exclusion) (Figure 4). For the case of the addition of Mo^{5+}, the reaction process only resulted in the formation of the aggregates of Mo oxides and silica nanoparticles. The high field strength of Mo ions may greatly influence the surrounding oxygen ions [21]. As the balance between dissolution and regrowth of silica plays a crucial role in the structural transformation to hollow spheres [10], the influence of Mo^{5+} on oxygen ions may inhibit the regrowth of silica. Moreover, the high cation field could also cause easy separation of Mo species from the silicate network. Hence, the doping of Mo in the silica framework and the formation of SHSs failed in this case.

3.3. Fabrication of multi-metallic doped SHSs

The above results inspired us to further explore the doping of multi-metals within SHSs by this strategy. The metal ions, capable of synthesizing M^{I}@SHS successfully, have been selected as promising candidates for multi-metallic doping. Based on a similar one-pot process, the two, three, or four metal ions were mixed in the dispersion of silica particles. As the metal ion concentration in the reaction solution may influence the structural nanofeatures of M@SHSs [20], the total mixing amount was adjusted to be the same as 0.1 mM.
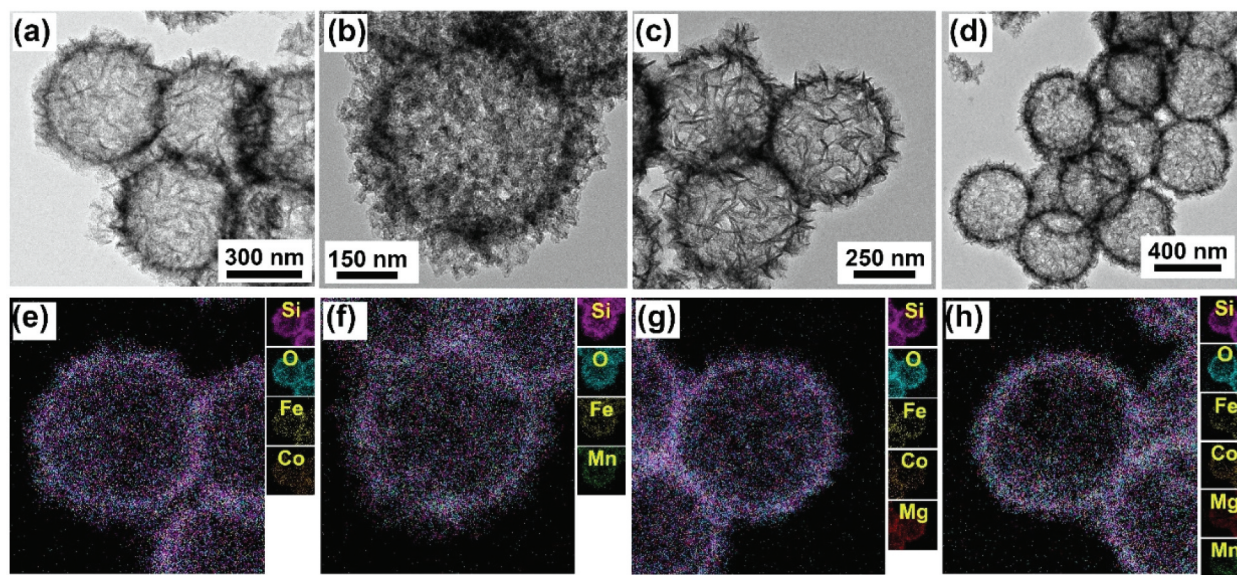
Figure 5. The TEM images of (a) FeCo@SHS, (b) FeMn@SHS, (c) FeCoMg@SHS, (d) FeCoMgMn@SHS. The corresponding elemental mappings of (e) FeCo@SHS, (f) FeMn@SHS, (g) FeCoMg@SHS, (h) FeCoMgMn@SHS.

The metal ions of Mn^{2+}, Fe^{2+}, Co^{2+}, and Mg^{2+}, whose doping mechanisms are through framework intercalation, have demonstrated the capability to create diverse multi-metallic doped SHSs. As shown in Figure 5, FeCo@SHS, FeMn@SHS, FeCoMg@SHS, and FeCoMgMn@SHS were all well-defined hollow spheres. No matter whether two, three, or four metals were mixed, the metals seemed homogenously distributed within the shells of the SHSs. We could hardly observe metal aggregates or nanoparticles in the TEM images. It implied the maintenance of the framework intercalation state of multi-metals in SHSs. The elemental mappings further confirmed the well-mixed states of various metals in the shells of the SHSs. Compared with single-metal doped SHSs, the SHSs with multi-metals displayed enhanced diffraction intensity in the XRD patterns (Figure S4), which might arise from the formed metal alloy oxides in the structure. For example, FeCo@SHS displayed a weak diffraction peak at 35.44°, which did not appear in the XRD patterns of Fe@SHS and Co@SHS. According to the JCPDS database, this newly appeared diffraction can be assigned from cobalt iron oxide (JCPDS No. 22–1086).

The chemical states of the metals in multi-metallic doped SHSs were further studied and compared by XPS measurements (Figure S5). The Si 2p spectrum of SHS without metals can be resolved into two components at 103.6 eV and 102.7 eV, attributed to the Si-OH and Si-O_x bonds, respectively [22]. A new peak, fitted at 101.7 eV, was observed in the Si 2p spectra of Fe@SHS, FeCo@SHS, FeCoMg@SHS, and FeCoMgMn@SHS. This peak could be attributed to the formation of Si-O-M as a result of silica framework doping with the metals. The O 1s spectra of Fe@SHS and FeCo@SHS had three main peaks at 533.3 eV, 532.1 eV, and 530.7 eV. The peaks of 533.3 eV and 532.1 eV should be attributed to the presence of Si-O-H and Si-O-Si bonds, while the peak at 530.7 eV likely arises from iron oxides or cobalt iron oxide in the silica frameworks. For FeCoMg@SHS and FeCoMgMn@SHS, an additional peak at 529.9 eV can be identified. It might imply the partial substitution of Si by Mg^{2+} in the M-O-Si lattices [23]. The Mg 1s spectra of FeCoMg@SHS and FeCoMgMn@SHS also supported above suggestion. Two fitted peaks were observed at binding energies of 1302.9 eV and 1303.8 eV [24,25], indicating the potential binding of Mg ions with silicate and other metal oxides in FeCoMg@SHS and FeCoMgMn@SHS. The Fe 2p spectra indicated that both Fe^{3+} and Fe^{2+} states presented in the Fe-doped SHSs. From the Co 2p spectra and Mn 2p spectrum, the Co and Mn states in the multi-metallic doped SHSs were determined to be Co^{2+} and Mn^{2+}, respectively. Based on the XPS analysis, we also estimated the metal contents in these M@SHSs. The total metal ratios were in the range of 5.9–8.7% (Table S1). The Fe/Co, Fe/Co/Mg and Fe/Co/Mg/Mn ratios for FeCo@SHS, FeCoMg@SHS, and FeCoMgMn@SHS were all near 1, which was well consistent with the additional ratios of metals.

The N_2 sorption isotherms of the above multi-metallic doped SHSs exhibited type IV isotherms, indicating a mesoporous structure. The pores were in the range of 3–9 nm. Due to the framework intercalation states, all these SHSs still possessed high specific surface areas (432–534 m^2/g) and pore volumes (0.95–1.13 m^3/g) (Table S1). Compared to the SHS and single-metal doped

SHSs, the surface areas and pore volumes of multi-metals doped SHSs were inclined to increase (Figure S6). The silica framework doping of the multi-metals may not only preserve the porous space within SHSs but also increase the nanotopographical roughness. It thus led to a higher surface area with more pore volume for multi-metallic-doped SHSs. From the FTIR spectra, the absorption peak from the siloxane network (around 1100 cm^{-1}) became narrower for multi-metals doped SHSs in contrast to single-metal doped SHSs (Figure S7). It implied that incomplete silica frameworks or structural defects of silica networks might be partially repaired through the doping of multi-metals.

3.4. Catalysis performance of multi-metallic-doped SHSs

The metal-doping effects in M@SHSs were studied and compared based on the degradation of acid orange 7 (AO7) with H_2O_2. It is known that multi-metals supported catalysis systems may have synergistic effects to enhance catalytic efficiency [26]. However, the relationship between the multi-metals doping and the synergistic effect for catalysis could hardly be understood and manipulated. The present one-pot synthesis of multi-metals doped SHSs provided a facile platform to study the synergistic effect with the similar Fe distribution state in the supports.

The degradation of AO7 relies on the hydroxyl and superoxide anion radicals produced from the active Fe ions with H_2O_2. AO7 solution shows a major adsorption peak at 484 nm in the UV-vis spectrum (Figure 6(a)). With the presence of Fe-containing M@SHSs and H_2O_2, the peak intensity of the AO7 solution will decrease with the reaction proceeding. The time-dependent intensity changes at 484 nm of various Fe-containing M@SHSs are shown in Figure 6(b). The order of the catalytic activity was FeCo@SHS>Fe@SHS>FeCoMgMn@SHS>FeCoMg@-SHS (Figures 6(c,d)). The Fe-based SHS doped with dual metals demonstrated superior catalytic activity, indicating an excellent synergistic effect. In contrast, the catalytic efficiencies of FeCoMg@SHS and FeCoMgMn@SHS were found to be significantly hindered, even lower than the single-metal doped Fe@SHS.

According to the Fenton reaction mechanism, the catalytic efficiency primarily determined by the reaction cycle from Fe^{2+} and Fe^{3+} ions with H_2O_2 [27–29]. Fe^{2+} may generate •OH radical and Fe^{3+} from H_2O_2 with a high reaction rate, while Fe^{3+} produces $•O_2^-$ radical and Fe^{2+} by reacting with H_2O_2 at a low rate. The $•O_2^-$ radical has a weaker oxidation ability than •OH [30]. Thus •OH radical plays a major role in
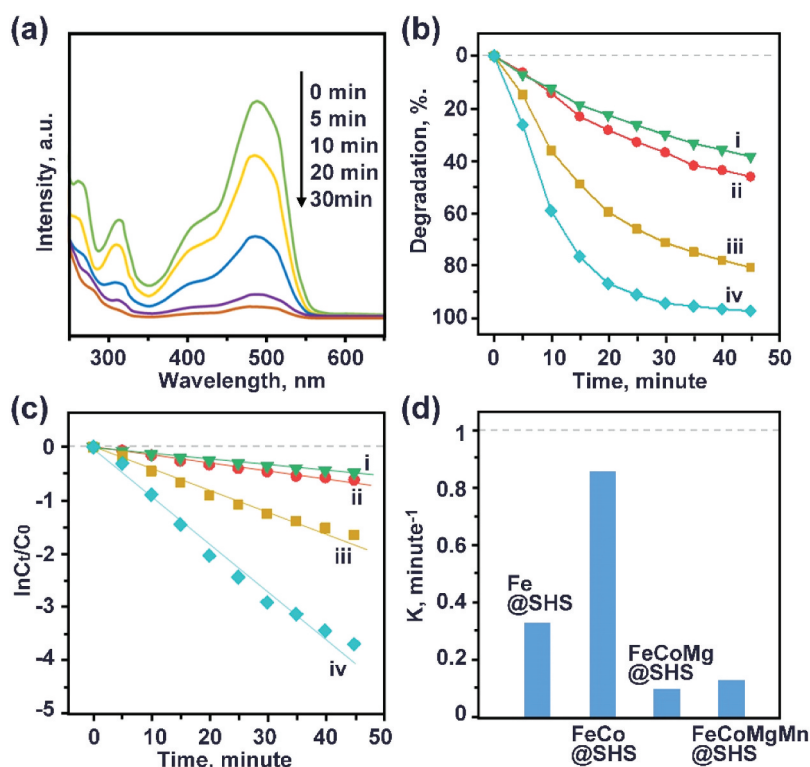

Figure 6. (a) The UV-vis spectra for the degradation of AO7 at different reaction times by using FeCo@SHS as the catalyst. (b) The time-dependent degradation percentage of AO7 based on the intensity changes at $\lambda = 484$ nm, and (c) the pseudo-first-order kinetic curves by using (i) FeCoMg@SHS, (ii) FeCoMgMn@SHS, (iii) Fe@SHS, and (iv) FeCo@SHS. (d) The kinetic rate constants of different Fe-based SHSs.
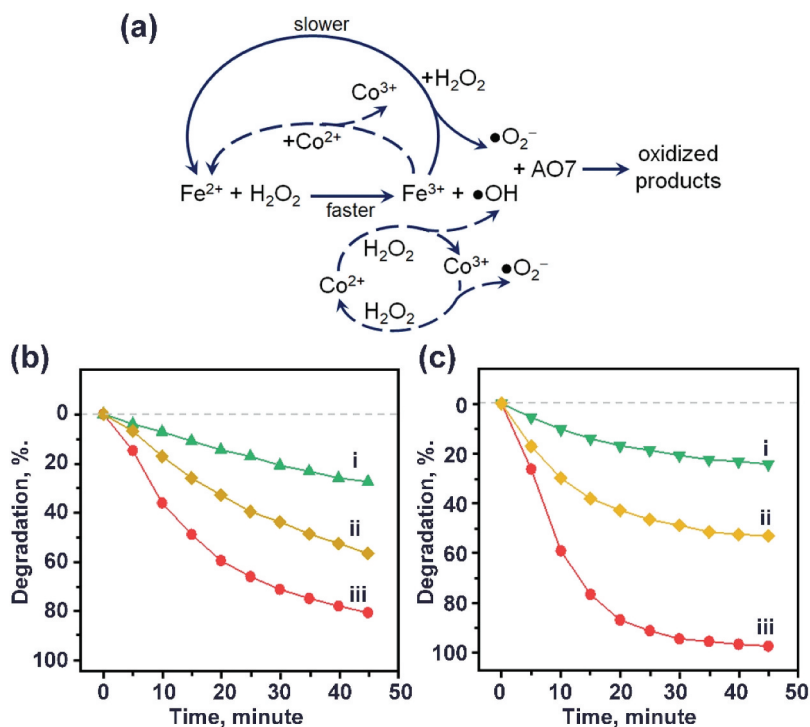
Figure 7. (a) The synergistic effect of Fe/Co co-doped catalysts for the degradation of AO7. The degradation percentage of AO7 by using (b) Fe@SHS and (c) FeCo@SHS as the catalysts in the presence of (i) isopropyl alcohol, (ii) 1,4-benzoquinone as radical quenchers, and (iii) without radical quencher.

accelerating the oxidation of AO7 in Fe-based catalysts. Co^{2+} may also produce $\bullet OH$ radical from H_2O_2 and its catalytic activity is less pH sensitive than Fe^{3+} [31–33]. Therefore, the co-doping of Fe and Co in the structure may facilitate the formation of faster catalytic cycles and continuously produce more reactive species during the reaction process (Figure 7(a)). The standard redox potentials of Fe^{3+}/Fe^{2+} and Co^{3+}/Co^{2+} are 0.77 V and 1.81 V, respectively. It implies that Co^{2+} has the ability to reduce Fe^{3+}. The synergistic effect from Fe-Co thus may enhance the generation of $\bullet O_2^-$ and $\bullet OH$ radicals (Figure 7(a)), which greatly improve the catalytic efficiency of AO7 oxidation.

To further prove the synergistic effect on the reactive oxidative species, quenching experiments were conducted with isopropyl alcohol (IPA) as the $\bullet OH$ quencher and 1,4-benzoquinone (BQ) as the $\bullet O_2^-$ quencher, respectively. For the case of Fe@SHS, the AO7 oxidation was inhibited by 67% when 3 mM IPA was added to the reaction system (Figure 7(b)). The oxidation efficiency was decreased by 31% in the presence of 3 mM BQ. It indicated that $\bullet OH$ radicals were the primary radical species for promoting AO7 oxidation. For Fe-Co@SHS, the AO7 oxidation efficiency was decreased by 75% and 45% with the addition of IPA and BQ in the system, respectively (Figure 7(c)). This result elucidated the production of more $\bullet O_2^-$ and $\bullet OH$ radicals in the Fenton oxidation process by using FeCo@SHS as the catalyst.

The lower catalytic activity of FeCoMg@SHS than FeCo@SHS should be because Mg^{2+} has a negligible effect on the generation of oxidative radicals. The intercalation of Mg within the silica framework could some extent repair the defects in the structure [17]. It thus decreased the surface area of the metal-doped SHS, which did not favor improving the catalysis efficiency. The lower catalysis performance of FeCoMg@SHS and FeCoMgMn@SHS might also be caused by the formation of various types of Mg alloy oxides. These alloy oxides may impede the electron transfer between active metal sites and restrict the synergistic effect. It thus led to a great decrease in catalysis efficiency for the triple-metallic, and quadruple-metallic doped SHSs.

4. Conclusions

Nanoarchitectured metal functionalized porous silica spheres were fabricated by a facile and general synthetic strategy. The metal-doped in M@SHSs (Co, Fe, Mg, and Mn) showed high homogeneous distribution states in the shell with good maintenance of hollow space in the structure. The comparison of the doping states of various metals elucidated that the successful silica framework intercalation and the hollow spherical transformation should rely on the formation of metal hydroxyl species in the reaction process and the proper cation field strength of the metals. Based on the multi-metallic doped SHSs, we studied the synergistic effect of metals on the catalytic oxidation of AO7. It showed the importance of proper metal combination on the catalytic efficiency. The best

catalytic performance of FeCo@SHS was due to that the co-doped Fe/Co could promote the continuous formation cycles for more active oxidative radicals. Through proper design of the doped metals in SHSs, the structures should find more applications in catalysis, drug delivery, and adsorption with unique and enhanced properties.

Acknowledgments

Disclosure statement

No potential conflict of interest was reported by the author(s).

Funding

References

[1] Hussain I, Sahoo S, Sayed MS, et al. Hollow nano- and microstructures: mechanism, composition, applications, and factors affecting morphology and performance. Coord Chem Rev. 2022;458:214429. doi: 10.1016/j.ccr.2022.214429

[2] Liu T, Zhang L, Cheng B, et al. Hollow carbon spheres and their hybrid nanomaterials in electrochemical energy storage. Adv Energy Mater. 2019;9 (17):1803900. doi: 10.1002/aenm.201803900

[3] El-Toni AM, Habila MA, Labis JP, et al. Design, synthesis and applications of core-shell, hollow core, and nanorattle multifunctional nanostructures. Nanoscale. 2016;8:2510–2531. doi: 10.1039/C5NR07004J

[4] Sanchez-Ballester NM, Rydzek G, Pakdel A, et al. Nanostructured polymeric yolk-shell capsules: a versatile tool for hierarchical nanocatalyst design. J Mater Chem A. 2016;4:9850–9857. doi: 10.1039/C6TA03311C

[5] Kang Y, Cretu O, Kikkawa J, et al. Mesoporous multimetallic nanospheres with exposed highly entropic alloy sites. Nat Commun. 2023;14(1):4182. doi: 10.1038/s41467-023-39157-2

[6] Bao Y, Shi C, Wang T, et al. Recent progress in hollow silica: template synthesis, morphologies and applications. Micropor Mesopor Mat. 2016;227:121–136. doi: 10.1016/j.micromeso.2016.02.040

[7] Li Y, Shi J. Hollow-structured mesoporous materials: chemical synthesis, functionalization and applications. Adv Mater. 2014;26(20):3176–3205. doi: 10.1002/adma.201305319

[8] Sharma J, Polizos G. Hollow silica particles: recent progress and future perspectives. Nanomaterials. 2020;10(8):1599. doi: 10.3390/nano10081599

[9] Zhang T, Zhang Q, Ge J, et al. A self-templated route to hollow silica microspheres. J Phys Chem C. 2009;113(8):3168–3175. doi: 10.1021/jp810360a

[10] Ji Q, Ishihara S, Terentyeva TG, et al. Manipulation of shell morphology of silicate spheres from structural evolution in a purely inorganic system. Chem - Asian J. 2015;10(6):1379–1386. doi: 10.1002/asia.201500098

[11] Park SS, Ha CS. Hollow mesoporous functional hybrid materials: fascinating platforms for advanced applications. Adv Funct Mater. 2018;28(27):1703814. doi: 10.1002/adfm.201703814

[12] Kankala RK, Zhang H, Liu CG, et al. Metal species-encapsulated mesoporous silica nanoparticles: current advancements and latest breakthroughs. Adv Funct Mater. 2019;29(43):1902652. doi: 10.1002/adfm.201902652

[13] Mitchell KKP, Liberman A, Kummel AC, et al. Iron(iii)-doped, silica nanoshells: a biodegradable form of silica. J Am Chem Soc. 2012;134 (34):13997–14003. doi: 10.1021/ja3036114

[14] Yoon CM, Lee S, Cheong OJ, et al. Enhanced electro-response of alkaline earth metal-doped silica/titania spheres by synergetic effect of dispersion stability and dielectric property. ACS Appl Mater Interfaces. 2015;7(34):18977–18984. doi: 10.1021/acsami.5b02388

[15] Qiao ZA, Zhang P, Chai SH, et al. Lab-in-a-shell: encapsulating metal clusters for size sieving catalysis. J Am Chem Soc. 2014;136(32):11260–11263. doi: 10.1021/ja505903r

[16] Sun J, Liu X, Tang Q, et al. Morphology adjustable silica nanosheets for immobilization of gold nanoparticles. ChemistrySelect. 2017;2 (20):5793–5799. doi: 10.1002/slct.201701004

[17] Zhao W, Sun J, Tang Q, et al. Atomic intercalation of magnesium in mesoporous silica hollow spheres and its effect for removal of dyes. Appl Surf Sci. 2020;507:144919. doi: 10.1016/j.apsusc.2019.144919

[18] Zhao W, Wang W, Meng F, et al. One-pot synthesis of bimetallic Fe/Co incorporated silica hollow spheres with superior peroxidase-like activity. Chin Chem Lett. 2023;34(7):107858. doi: 10.1016/j.cclet.2022.107858

[19] Ji Q, Guo C, Yu X, et al. Flake-shell capsules: adjustable inorganic structures. Small. 2012;8 (15):2345–2349. doi: 10.1002/smll.201200317

[20] Zhao W, Fu Y, Chen Y, et al. Effective fenton catalyst from controllable framework doping of Fe in porous silica spheres. Micropor Mesopor Mat. 2021;312:110704. doi: 10.1016/j.micromeso.2020.110704

[21] Szumera M. Structural investigations of silicate-phosphate glasses containing MoO$_3$ by FTIR, Raman and 31P MAS NMR spectroscopies. Spectrochim. Acta Part A. 2014;130:1–6. doi: 10.1016/j.saa.2014.03.052

[22] Karamikamkar S, Abidli A, Behzadfar E, et al. The effect of graphene-nanoplatelets on gelation and structural integrity of a polyvinyltrimethoxysilane-based aerogel. RSC Adv. 2019;9(20):11503–11520. doi: 10.1039/C9RA00994A

[23] Zhang X, Gao X, Dong Y, et al. Nanoporous Mg-doped SiO$_2$ nanoparticles with tunable infrared emissivity toward effective radiative cooling coatings. J Alloys Compd. 2023;940:168905. doi: 10.1016/j.jallcom.2023.168905

[24] Chen H, Du X, Wu R, et al. Facile hydrothermal synthesis of porous $MgCo_2O_4$ nanoflakes as an electrode material for high-performance asymmetric supercapacitors. Nanoscale Adv. 2020;2(8):3263–3275. doi: 10.1039/D0NA00353K

[25] Hou F, Gorthy R, Mardon I, et al. Protecting light metal alloys using a sustainable plasma electrolytic oxidation process. ACS Omega. 2022;7(10):8570–8580. doi: 10.1021/acsomega.1c06442

[26] Kim UB, Jung DJ, Jeon HJ, et al. Synergistic dual transition metal catalysis. Chem Rev. 2020;120 (24):13382–13433. doi: 10.1021/acs.chemrev.0c00245

[27] Voinov MA, Pagán JOS, Morrison E, et al. Surface-mediated production of hydroxyl radicals as a mechanism of iron oxide nanoparticle biotoxicity. J Am Chem Soc. 2011;133(1):35–41. doi: 10.1021/ja104683w

[28] Sun M, Chu C, Geng F, et al. Reinventing fenton chemistry: iron oxychloride nanosheet for pH-insensitive H_2O_2 activation. Environ Sci Technol Lett. 2018;5(3):18–191. doi: 10.1021/acs.estlett.8b00065

[29] Wang S. A comparative study of fenton and fenton-like reaction kinetics in decolourisation of wastewater. Dyes Pigm. 2008;76(3):714–720. doi: 10.1016/j.dyepig.2007.01.012

[30] Hartmann M, Kullmann S, Keller H. Wastewater treatment with heterogeneous fenton-type catalysts based on porous materials. J Mater Chem. 2010;20:9002–9017. doi: 10.1039/c0jm00577k

[31] Lin LS, Song J, Song L, et al. Simultaneous fenton-like ion delivery and glutathione depletion by MnO_2-based nanoagent to enhance chemodynamic therapy. Angew Chem Int Ed. 2018;57(18):4902–4906. doi: 10.1002/anie.201712027

[32] Yang Z, Shan C, Pignatello JJ, et al. Mn(ii) acceleration of the picolinic acid-assisted fenton reaction: new insight into the role of manganese in homogeneous fenton AOPs. Environ Sci Technol. 2022;56 (10):6621–6630. doi: 10.1021/acs.est.1c08796

[33] Leonard S, Gannett PM, Rojanasakul Y, et al. Cobalt-mediated generation of reactive oxygen species and its possible mechanism. J Inorg Biochem. 1998;70(3–4):239–244. doi: 10.1016/S0162-0134(98)10022-3